

Study of the reaction  $\psi' \rightarrow \gamma\gamma J/\psi$

M. Oreglia,\* E. Bloom, F. Bulos, R. Chestnut, J. Gaiser,  
G. Godfrey, C. Kiesling,† W. Lockman, and D. L. Scharre  
Stanford Linear Accelerator Center, Stanford University, Stanford, California 94305

R. Partridge, C. Peck, and F. C. Porter  
Physics Department, California Institute of Technology, Pasadena, California 91125

D. Antreasyan, Yi-Fan Gu,‡ W. Kollmann,§ M. Richardson, K. Strauch, and K. Wacker  
Lyman Laboratory of Physics, Harvard University, Cambridge, Massachusetts 02138

D. Aschman,|| T. Burnett,¶ C. Newman, M. Cavalli-Sforza, D. Coyne, and H. Sadrozinski\*\*  
Physics Department, Princeton University, Princeton, New Jersey 08540

R. Hofstadter, I. Kirkbride, H. Kolanoski,†† K. Königsmann,  
A. Liberman,‡‡ J. O'Reilly,§§ B. Pollock, and J. Tompkins  
Physics Department and High Energy Physics Laboratory, Stanford University, Stanford, California 94305

(Received 9 December 1981)

The Crystal Ball detector at SPEAR has been used to investigate the decays  $\psi' \rightarrow \gamma\gamma J/\psi$ ,  $J/\psi \rightarrow (e^+e^- \text{ or } \mu^+\mu^-)$  resulting from production of  $8 \times 10^5 \psi'$ . From this selection of the data we measure the branching ratios for the processes  $\psi' \rightarrow (\eta \text{ or } \pi^0) J/\psi$  and  $\psi' \rightarrow \gamma\chi$ ,  $\chi \rightarrow \gamma J/\psi$ . An analysis of the angular correlations in the latter process furnishes measurements of the  $\chi(3.55)$  and  $\chi(3.51)$  spins and of the multipole structure of the radiative transitions.

I. INTRODUCTION

Charmonium as devised by Appelquist and Politzer<sup>1</sup> in their celebrated model describes a meson system formed by a  $c\bar{c}$  quark pair bound in a central potential. Because the charmed quark is so heavy, the system appears to be sufficiently nonrelativistic that the Schrödinger equation can be used to describe the bound states shown in Fig. 1. The mass of the  $2^3S_1$  state (radial quantum numbers are used in the notation employed here) lies below that for two charmed  $D$  mesons; therefore, with the Okubo-Zweig-Iizuka rule, there is a relative enhancement of radiative decays among the  $1^1S_0$ ,  $1^3S_1$ ,  $2^1S_0$ ,  $2^3S_1$ ,  $1^1P_1$ , and  $1^3P_{012}$  bound states. While the  $\psi'(3684)$  and  $J/\psi(3095)$  are well established<sup>2</sup> as the  $3S_1$  states, quantum numbers have been assigned to candidates<sup>3,4</sup> for the  $1^3P_{012}$  states on a weaker basis. A candidate for the  $1^1S_0$  state has been observed<sup>5,6</sup> at a mass of  $2978 \text{ MeV}/c^2$ . Two candidates for the  $2^1S_0$  state have been reported at masses of  $3455$  (Ref. 3) and  $3591$  (or  $3180$ )  $\text{MeV}/c^2$  (Ref. 7). More recently, a new can-

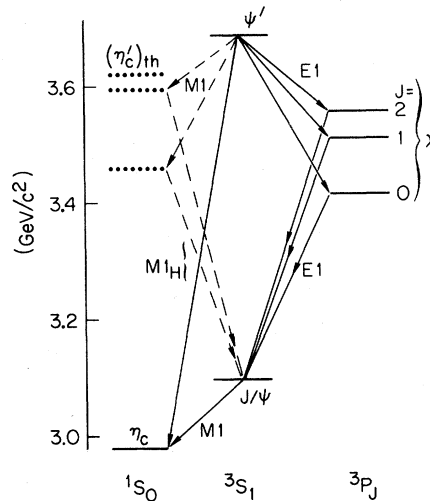


FIG. 1. The charmonium levels. Putative levels and transitions not confirmed in this experiment are indicated by broken lines;  $(\eta'_c)_{th}$  denotes the level expected for the  $2^1S_0$  level from the charmonium model.  $M1_h$  denotes a hindered M1 transition.

didate for the  $2^1S_0$  state having a mass of 3592 MeV/ $c^2$  has been observed<sup>8</sup> in the inclusive photon spectrum of decays of the  $\psi'$ .

A study of the charmonium system by means of the cascade sequence  $\psi' \rightarrow \gamma\chi$ ,  $\chi \rightarrow \gamma J/\psi$ , where  $\chi$  is a  $^1S_0$  or  $1^3P_j$  state and the  $J/\psi$  is analyzed by its decay into  $l^+l^-$  ( $e^+e^-$  or  $\mu^+\mu^-$ ), provides a largely background-free method for identifying these bound states. Additionally, an analysis of the angular correlations in the cascade final state permits a direct measurement of the  $\chi$  spin and of the multipole coefficients describing the two individual radiative transitions. The decay  $\psi' \rightarrow \eta J/\psi$ ,  $\eta \rightarrow \gamma\gamma$  exhibits the same topology as the cascade reaction; this process is therefore studied in order to separate it from the  $\chi$  events. In addition, the decay  $\psi' \rightarrow \pi^0 J/\psi$ , forbidden by isospin symmetry, is observed.

In the experiment reported here a large-solid-angle nonmagnetic detector having a high efficiency and resolution for photons (the Crystal Ball detector) is used to study the  $\gamma\gamma l^+l^-$  final states resulting from  $(7.8 \pm 0.8) \times 10^5$   $\psi'$  decays at SPEAR. The data used for the work reported here were accumulated during four running cycles with a total running time of six weeks. During this period  $1518 \text{ nb}^{-1}$  of integrated  $e^+e^-$  luminosity was acquired. A search is made for new states in the charmonium system, an attempt is made to confirm the  $2^1S_0$  candidates previously reported, and the quantum numbers of the  $1^3P_{12}$  candidates are established.

## II. THE DETECTOR

### A. General layout

The Crystal Ball apparatus, shown in Fig. 2, is a large-solid-angle, nonmagnetic detector with excellent photon and electron measurement capabilities. The beam pipe at the SPEAR interaction region consists of an aluminum tube 110 mm in diameter and having a wall thickness of 1.65 mm. This thickness corresponds to 1.9% of a radiation length ( $L_{\text{rad}}$ ) at normal incidence and 4.3%  $L_{\text{rad}}$  at the limit of the central charged-particle tracking chambers where  $\cos\theta = 0.9$  ( $\theta$  is the polar angle with respect to the positron axis  $\hat{z}$ ). Rigidly mounted about the SPEAR beam pipe is a central tracking chamber system surrounded by two hemispherical arrays of NaI(Tl). Beyond the main NaI(Tl) arrays and near the beam pipe are smaller end-cap arrays of NaI(Tl) and spark chambers, fol-

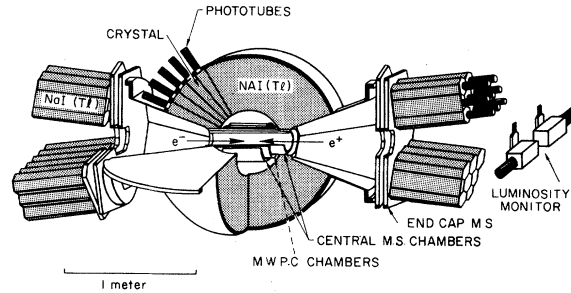


FIG. 2. Schematic of the detector.

lowed by the luminosity monitor counters. Finally, on either side of all these elements are the two arms of the outer hadron-muon separator (OHMS), consisting of slabs of iron interspersed with proportional chambers and scintillation counters, and covering 15% of the  $4\pi$  solid angle. These OHMS arms are not shown in Fig. 2 as this part of the apparatus is not used in the analysis presented here.

### B. Crystal Ball proper

At the heart of the apparatus is the ball proper, a segmented spherical shell with an inner radius of 10 in. and an outer radius of 26 in. consisting of 672 optically isolated NaI(Tl) crystals. Fabrication of the crystals was performed in collaboration with the Harshaw Chemical Company in their Solon, Ohio plant. Each crystal is about 16 in. or  $15.7L_{\text{rad}}$ , long and prismatic in shape, with a small end dimension of about 2 in. and a large end of about 5 in.; it is viewed by a 2-in. phototube.<sup>9</sup> The crystals were stacked to form two mechanically separate hemispheres, one upper and one lower. As demonstrated in Fig. 3, a 20-sided regular polyhedron, or icosahedron, forms the basis for construction of the two hemispheres. The major triangles of the icosahedron are subdivided into four smaller minor triangles to form a more spherical object; the minor triangles in turn are subdivided into nine actual crystals. Eleven distinct crystal shapes were required to achieve a nearly spherical stack. In order to permit entry of the  $e^+$  and  $e^-$  beams the 48 crystals nearest the beam ( $z$ ) axis were removed, leaving 94% of the  $4\pi$  solid angle covered. The "equator" shown in Fig. 3 demarcates the boundary of the two hemispheres; the terms "tunnel region" and "tunnel modules" refer to the first layer of crystals surrounding the beam entries.

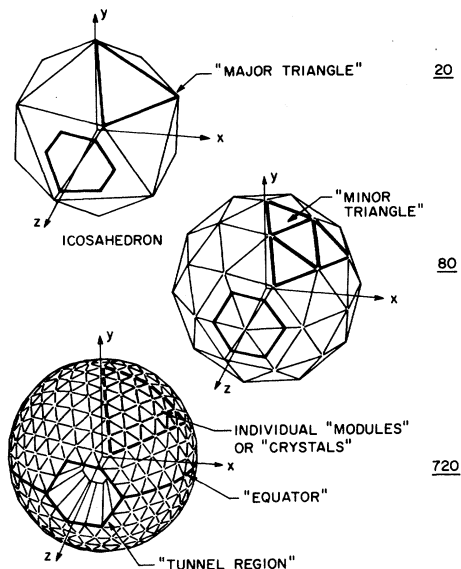


FIG. 3. Development of the ball geometry and nomenclature.

Each crystal was hand-sanded (“compensated”) so that the light received by the phototube at the large end of the crystal would be as independent as possible of the shower position in the module. Pieces of white reflector paper were then fitted against each face of each crystal, followed by a sheath of aluminized material for the purpose of optically isolating each crystal from its neighbors. Light produced by a crystal reaches its phototube by way of two air gaps, each approximately 1 in. long and separated by a 0.5-inch-thick window which serves as part of the hermetic seal. Compared to a direct (greased) optical coupling, a 60% loss of photons resulting from a 0.66-MeV shower is realized with the air-gap arrangement. Construction details and stacking data can be found in Ref. 10.

### C. End caps

Also shown in Fig. 2 are the NaI(Tl) end caps. These consist of 60 hexagonal crystals, 48 of which are  $20L_{\text{rad}}$  long (12 of them are  $10L_{\text{rad}}$ ) and 6 in. across at the widest transverse dimension. Each end-cap crystal is hermetically sealed in a stainless-steel can and viewed by a 3-in. phototube greased directly onto the rear window of the can. The end caps bring the total NaI(Tl) solid-angle coverage to 98% of  $4\pi$ . In the analysis presented here the end caps were not used to reconstruct

tracks; rather, they served to detect the presence of photons and charged particles over most of the  $4\pi$  solid angle, and so to reject events having any particles beyond the tunnel region.

### D. Charged-particle tracking chambers

A four-stage system of charged-particle tracking chambers complements the NaI(Tl) portion of the detector. The system, shown in Fig. 2, consists of three central cylindrical chambers about the beam pipe at the interaction region, and the planar end-cap chambers. Working outward from the interaction region, a particle first traverses a spark chamber with magnetostrictive (MS) readout, followed by a multiwire proportional chamber (MWPC), and finally another spark chamber. A track perpendicular to the beam axis travels through  $0.015L_{\text{rad}}$  of chamber construction material before reaching the outermost spark-chamber gap. This material, together with that in the beam pipe, resulted in a  $\gamma$ -conversion loss of 5% of the events relevant to this work. Proportional-chamber information is primarily useful for purposes of triggering and charged-particle identification, while the spark chambers are used to reconstruct charged-particle trajectories.

The proportional chambers operate on a gas mixture of 90% Ar/10% CO<sub>2</sub> and appear as a cylindrical shell of inner radius 90 mm, outer radius 115 mm, and an active length of 338 mm, corresponding to an effective coverage of 84% of  $4\pi$  sr. Two separate chambers comprise the proportional chamber system. Each chamber consists of 144 gold-plated tungsten sense wires oriented along the beam axis, 0.02 mm in diameter and with an inter-wire spacing of about 4.5 mm. Separated from the wires by a 5.0-mm gap are two cathode planes on either side of the wires; one plane is solid while the other consists of 36 strips. Relevant features are described in Table I, and construction and performance details for the chambers can be found in Ref. 11.

The two central spark chambers<sup>12</sup> each have two gaps and a solid-angle coverage of 94% of  $4\pi$  sr for the innermost chamber and 71% of  $4\pi$  sr for the outermost chamber; since sparks in both chambers are required for a chamber-reconstructed trajectory, the latter acceptance applies to such reconstructions. Dimensions and orientations of the spark-chamber planes appear in Table I. The overall accuracy for locating the position of a spark on a strip is 0.3–0.5 mm; two sparks on the

TABLE I. Charged-particle tracking-chamber specifications (dimensions are in millimeters).

Chamber	Plane: radius/length	spacing	Strip or wire width	orientation	
Inner Spark	1	69/598	1.0	0.3	-30°
	2	79/598	1.0	0.3	0°
	3	79/598	1.0	0.3	0°
	4	89/598	1.0	0.3	+30°
MWPC	5	92/338	8.0	7.0	+62°
	6	97/338	4.0	.02	0°
	7	108/338	4.5	.02	0°
	8	113/338	9.0	7.0	+90°
Outer Spark	9	127/312	1.0	0.3	-45°
	10	137/312	1.0	0.3	0°
	11	137/312	1.0	0.3	0°
	12	148/312	1.0	0.3	+45°

same strip are resolvable if separated by 3.0 mm or more. Augmenting the central chambers are two pairs of planar end-cap spark chambers,<sup>13</sup> also having two gaps in each chamber. These chambers are located just in front of the end-cap crystals in the  $x$ - $y$  plane (in the SPEAR coordinate system  $\hat{y}$  is oriented vertically and  $\hat{z}$  follows the positron orbit). All the spark chambers are pulsed at approximately 4.5 kV and operate on a mixture of 90% Ne/10% He gas; a pulsed ion-clearing field creates 25 msec of dead time.

### E. Triggers

The overall trigger is designed to minimize the acceptance of beam-gas, degraded-electron, and cosmic-ray events. Any one of four separate trigger elements is permitted to accept an event, and each element is adjusted to a level which can accommodate a reasonable data rate of 3–4 Hz at maximum luminosity. There are 40 msec of hold time for each event, corresponding to a 12% dead time at a 3-Hz trigger rate. A key feature in the success of all the trigger elements is the linear response of the phototube/electronics system to NaI(Tl) signals over the 0–4 GeV range, and the 3% gain stability of this system. There is considerable overlap of the four trigger systems, so that the total 3–4 Hz data rate is much smaller than

the sum of the four individual rates. The combined trigger efficiency for the  $\gamma\gamma\mu^+\mu^-$  or  $\gamma\gamma e^+e^-$  final state from  $\psi' \rightarrow \gamma\gamma J/\psi \rightarrow \gamma\gamma l+l^-$  exceeds 99% provided that all the particles in the final state are detected within the solid angle defined by  $|\cos\theta| < 0.84$ . All rates listed in the following discussion are for an energy  $E_{c.m.} = 3684$  MeV, a current  $I_b = 8$  mA, an instantaneous luminosity  $L = 1.1 \mu\text{b}^{-1}\text{sec}^{-1}$ , and a total trigger rate of 3 Hz.

The first and most general of the triggers is a total energy trigger. It fires if the analog sum of the NaI(Tl) modules comprising the ball proper, but not the end caps or tunnel modules, exceeds 1000–1100 MeV. An additional requirement that the trigger signal occur within  $\pm 20$  nsec of the beam-crossing signal from the SPEAR master oscillator (this indicates the moment of colliding beams) is common to all the trigger elements. The solid angle over which this trigger is effective is 84% of  $4\pi$  sr, and a contribution of about 0.9 Hz to the data rate is realized. This trigger reliably fires for the  $\gamma\gamma e^+e^-$  final state, but is somewhat inefficient in detecting  $\gamma\gamma\mu^+\mu^-$  due to the low total energy deposited by the minimum-ionizing muons in this final state, together with the uncertainty in the hardware energy calibration.

A secondary topology trigger makes use of the separate energy signals in the hemispheres. The signals from each hemisphere are routed through threshold discriminators set at 144 MeV, which

corresponds to the lower edge in the energy distribution of minimum-ionizing particles traversing the ball radially (see Sec. III). It is required that the two hemisphere signals be received within 20 nsec of each other in order to reduce the cosmic-ray rate. Also included in the coincidence is the full ball energy signal (i.e., the energy obtained by summing all the crystals in the ball proper) which is required to exceed 650 MeV; this provides the total energy condition in this trigger. It is further required that the full ball signal occur within  $\pm 8$  nsec of the beam-crossing signal. The tunnel modules are included in this trigger, which therefore fires for many Bhabha electrons and beam-gas events. The secondary topology trigger typically contributes 1.2 Hz to the total trigger rate.

A third trigger is based upon charged-particle multiplicity and is also quite effective in detecting the  $\gamma\gamma\mu^+\mu^-$  state; it fires if two or more of the energy sums formed by crystals in major triangles exceed the minimum-ionizing threshold. Major triangle energies formed from analog signals from the NaI(Tl) are converted to logic pulses corresponding to 0, 1, 2, 3, or  $\geq 4$  major triangles (MT) exceeding the MT discriminator threshold of 140 MeV. The  $\geq 4$ MT signal causes a trigger without further conditions; information from the 2MT and 3MT signals is considered only in conjunction with information from the multiwire proportional chambers. Groups of eight wires from the inner and outer chambers are ORED together in hardware to form 18 fixed "segments" in each chamber. Each segment from the inner chamber is then ANDed with the corresponding (i.e., same  $\phi$  value) segment in the outer chamber; if the AND is asserted a charged-particle hit is established; this logic signal is then ANDed with both the 2MT and 3MT signals to test for a charged-track trigger. The active solid angle for the system is limited to the 84% of  $4\pi$  covered by the proportional chambers. The multiplicity trigger is responsible for a contribution of 1.5 Hz to the data rate.

Finally, there is a trigger designed to respond to the energy-loss signals from back-to-back particles of high momentum and having a charge less than that of the electron. Here a signal for an energy exceeding 40 MeV must be observed in back-to-back minor triangles; in addition, the total energy measured by all crystals, excepting tunnel modules and end caps, must exceed 140 MeV. Bhabha electrons which satisfy these trigger conditions are responsible for most of the rate observed in this trigger element.

### III. ENERGY MEASUREMENT AND PARTICLE TRACKING

Raw data from the photomultipliers are recorded on tape in the form of two 13-bit numbers from two analog-to-digital converter (ADC) channels<sup>14</sup>; the low channel records energies in the range 0–160 MeV, while the input signal into the high channel is attenuated by a factor of 20 to cover the 0–3200 MeV range. Sources of monochromatic photons or electrons of several energies are required to calibrate the large dynamic range: the 0.66-MeV  $\gamma$  line from <sup>137</sup>Cs, the 6.13-MeV  $\gamma$  line from the decay of excited <sup>16</sup>O (obtained from the reaction <sup>19</sup>F( $p, \alpha$ )<sup>16</sup>O\* using 0.34-MeV protons from a Van de Graaff accelerator), and the high-energy Bhabha electrons produced at SPEAR. Over the 0–3200 MeV dynamic range the phototube and electronics network were measured to be linear to 1.5%.

Electrons and photons produced at SPEAR energies deposit more than 98% of their energy in the NaI(Tl). Associated with the particle's trajectory is the particular NaI(Tl) module which it hits, referred to as the "central module"; for showering particles this crystal usually measures a larger energy deposition than any of the nearby modules,<sup>15</sup> and typically it contains more than 50% of the total shower energy. The stacking geometry of the crystals naturally forms a cluster of 12 crystals about the central module; the sum of energies in this cluster and the central crystal is used as one measure of the total shower energy. This standard  $\sum 13$  energy measurement configuration subtends 1.8% of the  $4\pi$  solid angle and measures 97.5% of the shower energy with a resolution  $\sigma = 0.028 \times E^{3/4}$  GeV (see Ref. 10). The pattern of energy deposited in the crystals is called the "profile."

Muons from the  $J/\psi$  decay form minimum-ionizing tracks, depositing an average energy of 208 MeV after traveling the full 16 in. length of a single crystal. Minimum-ionizing tracks provide an outstanding signature in that only a single crystal will "illuminate" (measure more than 10 MeV) if the track is fully contained in the one crystal. Tracks originating at a displaced interaction vertex will not traverse the ball radially and may illuminate up to three crystals. In addition, there is some multiple scattering and  $\delta$ -ray production, so that up to four crystals may be illuminated by a high-momentum muon. Figure 4 shows the results of a study of muons from the decay  $\psi' \rightarrow \gamma\chi(3.51)$ ,

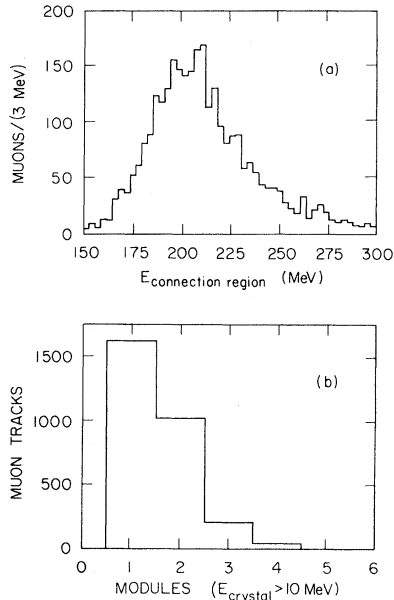


FIG. 4. Study of muon characteristics from  $\psi' \rightarrow \gamma\chi(3.51) \rightarrow \gamma\gamma\mu^+\mu^-$ . (a) The distribution of the total energy in a cluster of contiguous NaI(Tl) crystals, where each contributing crystal is required to measure more than 10 MeV. (b) The distribution of the number of crystals (modules) in these connected regions.

$\chi \rightarrow \gamma J/\psi$ ,  $J/\psi \rightarrow \mu^+\mu^-$ . Since these muons possess minimum-ionizing energy, the muon-identification algorithm for this study was (1) track energy between 150 and 280 MeV, (2) one to four crystals registering an energy greater than 10 MeV each, and (3) the track is charged (see below).

Of the charged hadrons, 60% interact and deposit a wide range of energies in NaI(Tl) (a crystal is one nuclear-interaction length long) by hadronic interactions with the nuclei in the crystal lattice, or by  $dE/dx$  ionization processes. Energy profiles from these reactions are quite unpredictable, producing large energy deposition regions of irregular shape and density. Such profiles can illuminate more than 13 crystals, often resulting in split patterns resembling those created by multiple tracks.

In Figs. 5 and 6 are Mercator-type projections of all modules comprising the ball proper, with the measured energy appearing for modules measuring more than 0.5 MeV; the projections are shown for some events from the decay  $\psi' \rightarrow \pi^0 J/\psi \rightarrow \gamma\gamma l^+ l^-$ . The photons from the decay of the  $\pi^0$  have the average opening angle in Fig. 5 and the minimum in Fig. 6. An overlap of the photon tracks in the latter figure is apparent, although the photons are still clearly resolved. For overlaps worse than this

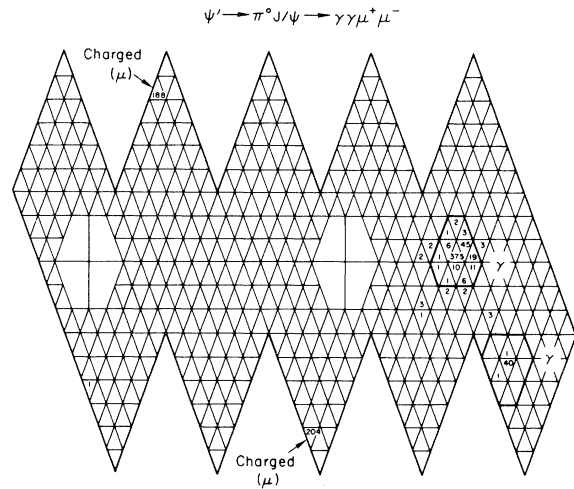


FIG. 5. Event map for  $\psi' \rightarrow \pi^0 J/\psi \rightarrow \gamma\gamma\mu^+\mu^-$  event. The energy is shown in MeV for all crystals having more than 0.5 MeV. If an energy cluster was associated with a charged-particle track in the charged tracking chambers the word “charged” appears. Also shown is the  $\sum 13$  cluster for each track.

$26^\circ$  opening-angle case fluctuations of the electromagnetic shower make it difficult to measure the individual energies accurately; therefore, we reject events having less than a  $26^\circ$  angle between any pair of particles.

Tracking of all photons and of the charged particles not reconstructed in the charged-particle tracking chambers requires isolation of the energy clusters (often overlapping) created by each particle. First, the isolated “connected regions” of all contiguous crystals, each crystal measuring more than 10 MeV, are identified; then each connected

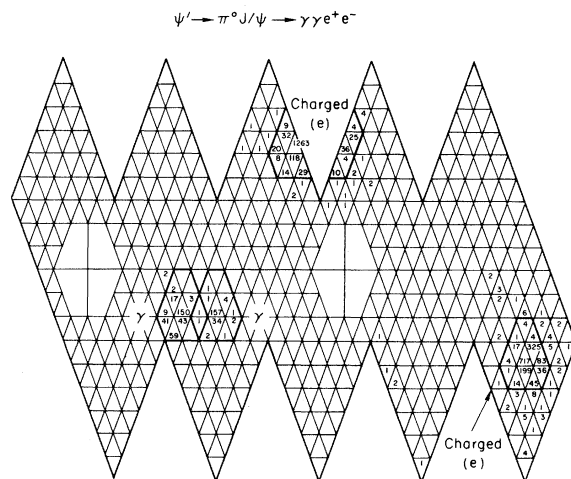


FIG. 6. Event map for  $\psi' \rightarrow \pi^0 J/\psi \rightarrow \gamma\gamma e^+ e^-$  event.

region is scanned for structure which indicates the presence of isolated or overlapping clusters. Significant structures in a connected region are called "bumps"; each bump should correspond to one incident particle. Since a 10-MeV threshold is applied to all crystals when searching for energy clusters, all tracks which are reconstructed must have deposited an energy exceeding about 20 MeV when one assumes that about half of the track energy appears in the central crystal. If the trajectory for a bump constructed in this manner coincides with one reconstructed using the spark chambers, or matches hits in the spark- and multiwire-proportional-chamber system, the particle is flagged as charged. Otherwise it is taken as a photon and, by applying pattern-recognition techniques to the shower profile, the position of an electromagnetically showering track can be determined to much better than the size of the central module. Shower fluctuations limit the accuracy of angles determined in this manner; the Crystal Ball has achieved a resolution  $\sigma = 1.5^\circ$  to  $2^\circ$  for photon and electron tracks reconstructed using the pattern-recognition technique. Energy dependence of this angular resolution is slight (see Ref. 10).

Only the inner and outer spark chambers are used in reconstructing charged tracks. In practice the direction cosines and vertex of each candidate charged track are fit independently, assuming that the actual interaction point was at the origin of the  $x$ - $y$  plane. A better measure of the event vertex is then obtained from a weighted average of the vertices determined from the fit of each track, followed by refitting of each track using this final vertex position. A tracking resolution of about  $1^\circ$  in both spherical angles is achieved using this procedure. A correlation of the leftover sparks, as well as of the multiwire proportional chamber information, with the NaI(Tl) pattern-recognition-reconstructed trajectories described previously, is employed to identify charged particles which fail to create a discernable path in the spark chambers; in these 14% of the  $\gamma\gamma l^+l^-$  events the trajectory for the charged particle not tracked by the spark chambers is determined from the NaI(Tl) profile, assuming a vertex at  $z=0$  if a vertex is not supplied by the other charged particle. A study of  $\psi' \rightarrow \gamma\chi \rightarrow \gamma\gamma e^+e^-$  events identified on the basis of energies and angles, but not charged particles, determined that the overall efficiency for detecting both leptons in a  $\gamma\gamma l^+l^-$  event is 96% over the central 90% of the solid angle.

Extreme fluctuation of the shower created by an

energetic photon or electron sometimes results in an energy profile which appears to result from two particles rather than one. A Monte Carlo simulation of photon and electron showers in the 10–1500 GeV range found that spurious tracks with an energy exceeding 40 MeV virtually never arise as a result of a split-profile type fluctuation. Neutral tracks of less than 40 MeV are therefore suspect if they form an opening angle of  $\cos\theta_{e\gamma} > 0.85$  (this angle corresponds to  $32^\circ$ , or about three crystal widths) with an electron which deposits 900 MeV or more in the crystals. Such suspect neutral tracks are eliminated from the event and their measured energy is added to that of the nearby  $e^\pm$ . The general  $26^\circ$  opening angle cut is sufficient to protect against overlap of photons with the highly compact muon energy clusters. Split profiles caused by hadronic interactions are not relevant to the work reported here.

#### IV. DATA ANALYSIS

##### A. Characteristics of the final state and event selection

The two photons in the decays  $\psi' \rightarrow \gamma\gamma J/\psi$ ,  $J/\psi \rightarrow l^+l^-$  can originate from the decay of an  $\eta$  or  $\pi^0$ , or from the cascade decay via an intermediate  $\chi$  state. For the reaction containing electrons a complete measurement of all energies is possible. The muonic final state deposits only about 320 to 560 MeV from the minimum ionizing particles, and about 550 MeV from the two photons. The photon energy range is safely smeared by 15% when determining the total energy acceptance windows, so that candidates for the  $\gamma\gamma J/\psi$  reaction are required to have a total measured energy of 792 to 1100 MeV for muonic and 3300 to 4200 MeV for electronic final states as a first selection criterion. Figure 7 shows the total energy distribution of events from the preliminary data tapes and indicates both the energy acceptance windows and the trigger thresholds. The first peak apparent in the figure at about 400 MeV is caused by minimum-ionizing particles accepted by the multiplicity trigger; the second "peak" at about 650 MeV is created by the total energy threshold of the secondary topology trigger. The broad structure centered at 2400 MeV is caused by hadronic interactions in the NaI(Tl). The total energy requirement accepted  $7 \times 10^5$  of the  $3 \times 10^6$  events from the raw data tapes.

The  $\gamma\gamma l^+l^-$  final-state topology is selected by

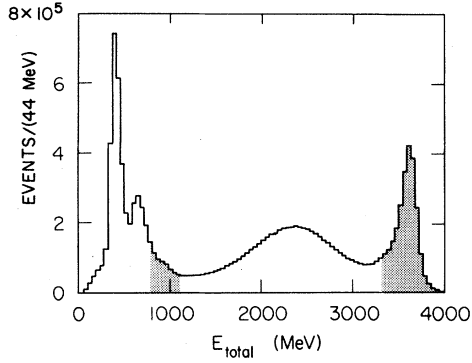


FIG. 7. Distribution of the total NaI(Tl) measured event energy before the general cuts (see text) were applied. The total-energy cuts for the  $e^+e^-$  and  $\mu^+\mu^-$  final states are indicated by shading.

requiring that (1) the event have only four tracks, (2) two of the tracks are neutral, and (3) two of the tracks are flagged as charged and appear either as an electron pair (each track deposited at least 900 MeV) or as a muon pair using the criteria discussed in Sec. III. In addition we require that the photon candidates deposit more than 40 MeV each

as an assurance that the measured photon energy is not contaminated by shower fluctuations from other particles in the final state. These topology cuts reduce the number of candidates to 4750.

To protect against accepting events having particles in the end-cap regions, the energy deposited in the end caps could not exceed 8 MeV; this value for the cutoff energy rejects 1% of the good events in which the end caps measure energy from shower fluctuation in the ball, and it reduced the candidate sample to 4433 events. A requirement that there be no reconstructed tracks in the ball having  $|\cos\theta| > 0.9$  further reduced the data sample to 3281 events. Finally, 2918 events satisfy a requirement that the opening angles  $\theta_{ij}$  between any two particles  $i$  and  $j$  exceed  $26^\circ$ . The cuts described up to this point are applied to all of the events comprising the  $\gamma\gamma l^+l^-$  data sample and shall henceforth be referred to as the “general cuts.”

The effects of the event-selection criteria on the efficiency for the acceptance of the various  $\gamma\gamma l^+l^-$  final states were obtained with a Monte Carlo study of the processes and are summarized in Table II. This table includes the effects of several cuts applied later in the analysis which are

TABLE II. Efficiencies.

State $s$ :		$ \cos\theta  < 0.9$	Cut for $\pi^0$	Remove $\eta$	C.L. $> 0.005$	Total
$\psi' \rightarrow s\psi \rightarrow \gamma\gamma\psi$		$\cos\theta_{ij} < 0.9$	(see text)	(see text)	(kinematic fitting)	
or		$E_{\text{track}} > 40 \text{ MeV}$				
$\psi' \rightarrow \gamma s \rightarrow \gamma\gamma\psi$		$E_{\text{end cap}} < 8 \text{ MeV}$				
			remove $\pi^0$ :			
$\chi(3.55)$	$e$	0.42	0.93	1.00	0.94	$0.370 \pm 0.015$
	$\mu$	0.47	0.93	1.00	0.94	$0.408 \pm 0.016$
$\chi(3.51)$	$e$	0.45	0.95	0.97	0.93	$0.387 \pm 0.011$
	$\mu$	0.50	0.95	0.97	0.93	$0.425 \pm 0.012$
$\chi(3.41)$	$e$	0.39	0.96	0.83	0.94	$0.295 \pm 0.007$
	$\mu$	0.44	0.96	0.83	0.94	$0.333 \pm 0.008$
$\chi(3.59)$	$e$	0.40	0.92	1.00	0.92	$0.338 \pm 0.008$
$J^P = 0^-$	$\mu$	0.45	0.92	1.00	0.93	$0.380 \pm 0.009$
$\chi(3.46)$	$e$	0.39	0.97	0.87	0.94	$0.306 \pm 0.007$
$J^P = 0^-$	$\mu$	0.43	0.97	0.87	0.94	$0.344 \pm 0.008$
$\eta$	$e$	0.48	1.00	0.00	0.94	$0.455 \pm 0.010$
	$\mu$	0.53	1.00	0.00	0.93	$0.497 \pm 0.011$
			include $\pi^0$ :			
$\pi^0$	$e$	0.39	0.88	1.00	0.94	$0.254 \pm 0.007$
	$\mu$	0.41	0.88	1.00	0.94	$0.276 \pm 0.007$

designed to separate  $\psi' \rightarrow (\eta \text{ or } \pi^0)J/\psi$  events from  $\chi$  cascade events; namely:  $m_{\gamma\gamma} = 135 \pm 25 \text{ MeV}/c^2$  for the  $\pi^0$  and  $m_{\gamma\gamma} > 525 \text{ MeV}/c^2$  for the  $\eta$  reaction. The C.L. efficiency column gives the effect of the confidence-level cut for the kinematic fitting of the events (Sec. IV D). The radiative decay multipole parameters affect the efficiencies obtained for the cascade reactions; pure dipole transitions were assumed when obtaining the values listed in the table, and the uncertainty in the efficiencies resulting from this assumption is included in the quoted errors. Other sources of uncertainty arise from surveying errors and uncertainty in knowledge of the detector performance.

Not shown in Table II is the 0.70 efficiency for the cut to remove cascade events from the  $\pi^0$  sample by rejecting the event if  $M_{\gamma J/\psi} = 3530 \pm 60$  or  $3411 \pm 5$ , if  $m_{\gamma\gamma} < 110$ , or if  $m_{\gamma\gamma} > 160 \text{ MeV}/c^2$ . Also not shown are the 0.95 and 0.96 efficiencies which account for photon-conversion losses and charged-particle-identification efficiency, respectively, for each  $\gamma\gamma l^+ l^-$  event. The latter efficiency is described in Sec. III.

### B. Event kinematics

Past studies<sup>3,4,7</sup> of the  $\gamma\gamma J/\psi$  final state resulting from the reaction

$$\psi' \rightarrow \gamma' \chi, \quad \chi \rightarrow \gamma J/\psi \quad (4.1)$$

have presented data in the form of a scatter plot of the  $\gamma J/\psi$  masses. The kinematic boundaries and the appearance of relevant states on the scatter plot are illustrated in Fig. 8(a). The outermost envelope of the scatter plot contains any  $\gamma J/\psi$  masses from the process  $\psi' \rightarrow \gamma\gamma J/\psi$ .<sup>16</sup> Doppler broadening of the photon cascading to the  $J/\psi$  causes the mass pairs to occupy either vertical or horizontal bands between the kinematic boundaries, depending on whether the higher or lower  $\gamma J/\psi$  mass is the correct monochromatic solution. The intrinsic resolution of the measuring apparatus smears the kinematically allowed regions on the figure. Decays of the form

$$\psi' \rightarrow m J/\psi, \quad m \rightarrow \gamma\gamma, \quad (4.2)$$

where  $m$  represents an  $\eta$  or  $\pi^0$  for instance, give rise to points on diagonal curves recessed from the envelope borders, with the  $\eta$  and  $\pi^0$  masses (indicated in the figure) very near the extremes; the density along these mass curves is nearly uniform. Identification of Doppler broadening and determination of the masses of  $\chi$  states is made difficult

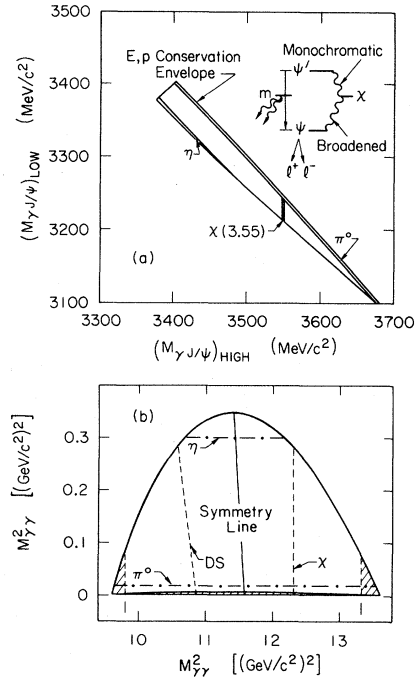


FIG. 8. Kinematic boundaries for  $\psi' \rightarrow \gamma\gamma J/\psi$  in the (a)  $(M_{\gamma J/\psi})_{\text{HIGH}}$  versus  $(M_{\gamma J/\psi})_{\text{LOW}}$  scatter plot, and (b) Dalitz plot. The shaded region in (b) indicates the areas obscured by the  $E_{\gamma} > 40 \text{ MeV}$  cut (the side lobes) and the  $26^\circ$  opening angle cut (bottom area). DS denotes the false solution reconstructed from the Doppler-shifted photon.

on the mass scatter plot because of an apparent broadening caused by the energy dependence of the NaI(Tl) energy resolution. The problem is avoided by presenting the data on a Dalitz plot [ $m_{\gamma\gamma}^2$  vs.  $M_{\gamma J/\psi}^2$ ] on which each event is plotted twice, once for each  $\gamma J/\psi$  mass about the symmetry line  $d(m_{\gamma\gamma}^2)/d(M_{\gamma J/\psi}^2) = -2$  (see Ref. 10). The kinematic boundaries for the Dalitz plot subject to the opening angle, photon energy, and acceptance cuts are shown in Fig. 8(b). Such a Dalitz plot contains information that is more easily interpreted than that in the  $M_{\gamma J/\psi}$  scatter plot; the Doppler-shift broadening is separated from the resolution effect by observing that the Doppler-shifted solution has a characteristic slope  $d(m_{\gamma\gamma}^2)/d(M_{\gamma J/\psi}^2) = -1$  [this is denoted by DS for  $\chi(3.51)$  in Fig. 8(b)].

### C. Signals and backgrounds

The two stronger  $\chi$  states and the  $\eta$  band can be seen in the  $M_{\gamma J/\psi}$  scatter plots of the unfitted  $e^+e^-$  and  $\mu^+\mu^-$  final states [Figs. 9(a), 9(b)]. The

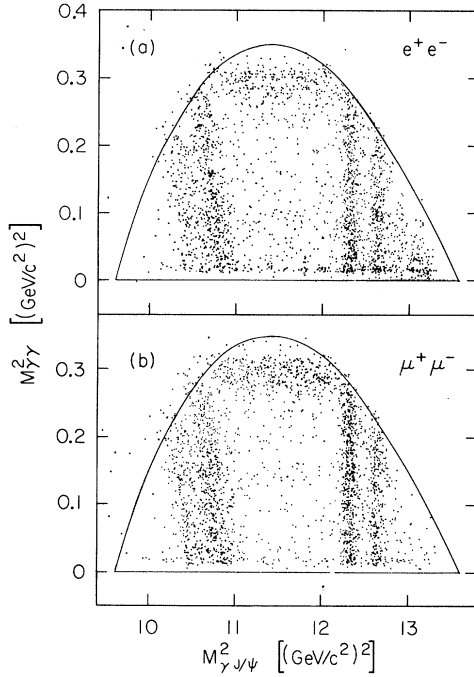


FIG. 9. Dalitz plots of (a)  $e^+e^-$  and (b)  $\mu^+\mu^-$  subsets of the unfitted preliminary event sample.

figure shows the 1598  $e^+e^-$  and 1320  $\mu^+\mu^-$  events which survive the general cuts described in Sec. IV A. Here  $M_{\gamma J/\psi}$  is obtained using one measured photon energy and the known  $\psi'$  mass. Though elongation of the  $\chi$  states would suggest Doppler broadening, the observed broadening is primarily a resolution effect, as explained in the previous section.

The neutral energy for the decays (4.1) or (4.2) is kinematically confined to the range  $542 < E_{\text{neutral}} < 589$  MeV. Imposing the requirement that the measured neutral energy exceed 490 MeV (this energy was determined to be a safe lower bound) on the events shown in Fig. 9 produces the cleaner Dalitz plot containing the 1206  $e^+e^-$  and 1280  $\mu^+\mu^-$  events shown in Fig. 10. The real and Doppler-shifted solutions for  $\chi(3.51)$  and  $\chi(3.55)$  are apparent in the Dalitz plot of unfitted data, as are the  $\eta$  and  $\pi^0$  decays.

The decays

$$\psi' \rightarrow \pi^0 \pi^0 J/\psi, \quad \pi^0 \rightarrow \gamma\gamma \quad (4.3)$$

in which two photons are undetected (or have energies less than 20 MeV) are the main source of the background. This source populates the lower  $M_{\gamma J/\psi}$  mass region (around  $3.4-3.5$  GeV/ $c^2$ ) since the  $\pi\pi$  mass distribution has been found to be

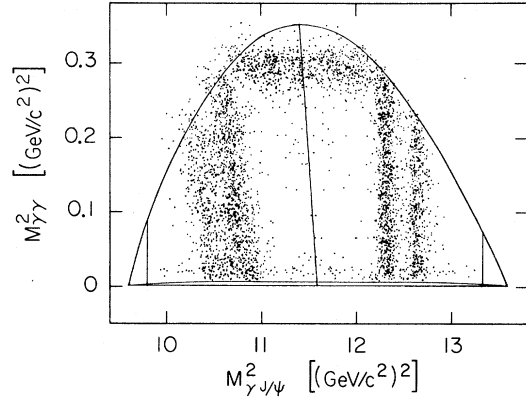


FIG. 10. Dalitz plot of the final event sample prior to kinematic fitting. The broad horizontal band at the top occurs at the  $\eta$  mass; that near the bottom occurs at the  $\pi^0$  mass. Two strong signals for  $\chi(3.51)$  and  $\chi(3.55)$  appear as vertical bands to the right of the symmetry line; the Doppler-shifted bands on the left of the symmetry line are tilted with a slope of  $-1$ .

enhanced at the high kinematic end.<sup>17,18</sup> This behavior is consistent with the Monte Carlo simulation of background from  $\pi^0\pi^0$  events which uses the measured  $\pi\pi$  mass distribution. After normalizing to the data sample, the Monte Carlo simulation of the  $\pi^0\pi^0$  background predicts 140 background events before kinematic fitting and after the  $E_{\text{neutral}} > 490$  MeV cut, none of these having  $m_{\gamma\gamma} < 200$  MeV/ $c^2$ .

Other sources of background arise from

$$\psi' \rightarrow \pi^+ \pi^- J/\psi, \quad J/\psi \rightarrow l^+ l^- \quad (4.4)$$

and

$$\psi' \rightarrow \pi^+ \pi^- \pi^0, \quad \pi^0 \rightarrow \gamma\gamma, \quad (4.5)$$

though the latter decay is exceedingly rare and contributes less than one event. Pions from reaction (4.4) may appear as photons due to charge detection inefficiency; these pions do not have sufficient energy to produce minimum-ionizing signals and therefore populate a broad region of the scatter plot in the high- $M_{\gamma J/\psi}$  areas. Fewer than 20 of these events survive the  $E_{\text{neutral}} > 490$  MeV cut.

Another source of background results from the QED process  $e^+e^- \rightarrow \gamma\gamma$  ( $e^+e^-$  or  $\mu^+\mu^-$ ), the probability of each radiation behaving as  $E_\gamma^{-1}$  (the QED process with final-state muons contributes even less). The background is found primarily in the low photon energy (high  $M_{\gamma J/\psi}$ ) region of the mass scatter plot. A Monte Carlo simulation of

the QED background agrees with the structure observed in the  $e^+e^-$  and  $\mu^+\mu^-$  plots, and predicts a background of fewer than two events after all cuts. These predicted QED events are neglected in the computation of rates. Other QED radiative processes, degraded SPEAR electrons, beam-gas collisions, and cosmic rays contribute background events only to the  $\psi'$  normalization sample; this is discussed in Sec. IV H.

#### D. Final data sample

The events in Fig. 10 are plotted on the  $M_{\gamma J/\psi}$  scatter plot [Fig. 11(a)] and the Dalitz plot [11(b)] after they have been kinematically fit to the hypothesis that they arise from  $\psi' \rightarrow \gamma\gamma J/\psi$ ; the fitting restricts all of the surviving events to fall within the envelope illustrated in Fig. 8(a). The  $\psi'$  and  $J/\psi$  masses are constraints in the fit, so that five-constraint (5C) and three-constraint (3C) fits are achieved for the electron and muon final states, respectively. The confidence-level distributions for both the  $e^+e^-$  and  $\mu^+\mu^-$  final states are flat for C.L.  $> 0.005$ ; this C.L. requirement is imposed on all fitted data and it applies to the 2234 events shown on Fig. 11. The apparent resolution for the low-resolution  $\gamma J/\psi$  masses is smaller in Fig. 11(b)

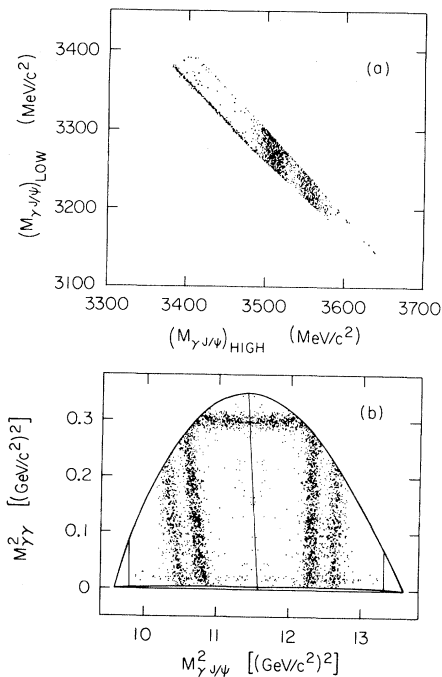


FIG. 11. Events after kinematic fitting in the (a) mass scatter plot and (b) Dalitz plot.

than in the unfitted plot (Fig. 10) because the kinematic fit reduces the absolute energy errors of the higher-energy photons to the values of those of the lower-energy photons (full width at half maximum = 18 MeV). After kinematic fitting all the surviving events were examined by a physicist; this examination identified six hadronic background events on the basis of highly irregular profiles. These events are eliminated from the final event sample.

#### E. $\psi' \rightarrow \eta J/\psi$

The  $m_{\gamma\gamma}$  distribution for all fitted events is shown in Fig. 12(a). Of the events in this figure, 412 candidates for the  $\eta$  events are separated from  $\chi$  and  $\pi^0$  events by using the cut  $m_{\gamma\gamma} > 525$  MeV/ $c^2$ ; the cut loses no  $\eta$  events but does admit some  $\chi(3.51)$  events into the  $\eta$  sample. The Monte Carlo simulation for  $\chi$  events (normalized to the  $\chi$  sample size) determines that 21  $\chi(3.51)$  events are included in the  $\eta$  sample. On the basis of another Monte Carlo simulation, 5  $\pi^0\pi^0$  background events are expected to be included in the  $\eta$  sample. Tests of the Monte Carlo model for backgrounds were made using the  $\eta$  data, and are reported in an earlier paper.<sup>18</sup>

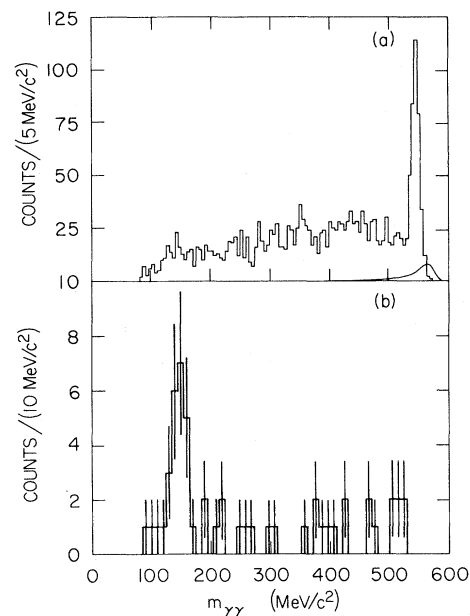


FIG. 12. Diphoton masses of fitted events. The solid line in (a) is the expected  $\pi^0\pi^0$  background magnified by 10. In (b) events have been removed from (a) if the higher  $\gamma J/\psi$  mass fell in a  $\chi$  region.

For our apparatus the mass distributions appear slightly non-Gaussian in shape even after kinematic fitting because of the non-Gaussian energy line shape of NaI(Tl) (Ref. 10). This introduces an uncertainty in the fitted mass value; for the  $\eta$  arising from reaction (4.2) this uncertainty is  $\pm 0.5$  MeV/ $c^2$ . There is an additional error on the fitted mass which arises from the uncertainty in the difference between the  $J/\psi$  and  $\psi'$  masses.<sup>19</sup> The value  $m_\eta = 547.3 \pm 0.5 \pm 0.9$  MeV/ $c^2$  is obtained from our data, where the first error is statistical and the second error covers the uncertainties described above. Our measured value compares well with the accepted value  $548.8 \pm 0.6$  MeV/ $c^2$ .<sup>20</sup> A width of  $\sigma = 1.2\%$  is obtained for the signal in the  $\gamma\gamma$  mass plot; this width compares well with the value of 1.0% predicted by our Monte Carlo simulation. The branching ratio for  $\psi' \rightarrow \eta J/\psi$  is computed in Sec. IV H.

#### F. $\psi' \rightarrow \pi^0 J/\psi$

Existence of the transition<sup>18,21</sup>  $\psi' \rightarrow \pi^0 J/\psi$  is apparent in the Dalitz plots of both fitted and raw data. A  $\pi^0$  signal is observed in the diphoton mass plot by removing the dominant background from cascade photons using a cut on the  $\gamma J/\psi$  masses. A subtraction of events from the  $m_{\gamma\gamma}$  plot [Fig. 12(a)] with  $(M_{\gamma J/\psi})_{\text{high}}$  in the ranges  $3410 \pm 5$  and  $3530 \pm 60$  MeV/ $c^2$ , and  $m_{\gamma\gamma} > 525$  MeV/ $c^2$ , results in the distribution shown in Fig. 12(b). The data in Fig. 12(b) in the mass range 0 to 525 MeV/ $c^2$  have been fitted to a Gaussian peak with a quadratic background distribution. The fit yields 23 events above background in the  $\pi^0$  peak, with eight background events having  $m_{\gamma\gamma} < 200$  MeV/ $c^2$ . A value of  $136.1 \pm 2.5 \pm 3.4$  MeV/ $c^2$  is obtained for the location of the peak (the first error is statistical and the second arises primarily from the  $J/\psi$ - $\psi'$  mass-difference uncertainty). A value of  $\sigma = (7.7 \pm 1.2)\%$  is obtained from the  $\gamma\gamma$  mass plot, which is consistent with the expected value of 6.8% for a low energy  $\pi^0$ . For  $m_{\gamma\gamma} < 200$  MeV/ $c^2$  and with the  $\chi$  cuts described above, the Monte Carlo simulations for  $\pi^0\pi^0$  and  $\chi$  backgrounds predict a total of five background events, in good agreement with the eight events observed. Less than one background event from the process (4.3) is expected in this mass region. Final lepton states for the pion transition are divided equally between electrons and muons (12 and 11, respectively).

There is some concern that the nonresonant process  $e^+e^- \rightarrow \pi^0 J/\psi$  (an electromagnetic process

which does not require conservation of isospin) may be responsible for the  $\pi^0 J/\psi$  events observed. The hypothesis is tested by searching for a similar transition at  $E_{\text{c.m.}} = 3772$  MeV ( $\psi''$ ). An analysis of  $1772 \text{ nb}^{-1}$  worth of data produced only one candidate for  $e^+e^- \rightarrow J/\psi$ ,  $J/\psi \rightarrow e^+e^-$ , giving a 90%-C.L.-upper-limit cross section of 0.06 nb. Nonresonant production should scale as  $E_{\text{c.m.}}^{-2}$ , implying an increase of 5% for the rate of the process between the  $\psi'$  and  $\psi''$  energies. A 90%-C.L. upper limit of 3.3 nonresonant events in the 23  $\pi^0$  events observed is obtained from the  $\psi''$  analysis. No correction for the nonresonant events is deemed necessary. [For the analogous nonresonant  $\eta J/\psi$  production, one expects the  $p$ -wave extrapolation  $B(e^+e^- \rightarrow \eta J/\psi) < (0.01 m_\pi^3 / m_\eta^3)\%$ , which represents a negligible correction to the resonant  $\eta J/\psi$  branching ratio.]

#### G. $\psi' \rightarrow \gamma\chi$ , $\chi \rightarrow \gamma J/\psi$

The distribution of the higher  $\gamma J/\psi$  mass solutions, after the application of all the cuts described in Table II, is shown in Fig. 13. In this  $\chi$  sample, 711 events arise from the  $e^+e^-$  final state and 793 events from the  $\mu^+\mu^-$  final state. The lower mass tail on the prominent  $\chi(3.51)$  peak in the  $\gamma J/\psi$  mass plot is slightly more pronounced for the  $e^+e^-$  final state. This is a result of the overlap of the 1 GeV electron showers with those of the 0.2 GeV photons, which causes a higher measured energy for these photons; this tail accounts for six events in the  $e^+e^-$  data sample in the 3.45–3.47-GeV/ $c^2$   $\gamma J/\psi$  mass region. Because of its cleaner nature, only the  $\mu^+\mu^-$  data sample is used to obtain an upper limit for the branching ratio of a

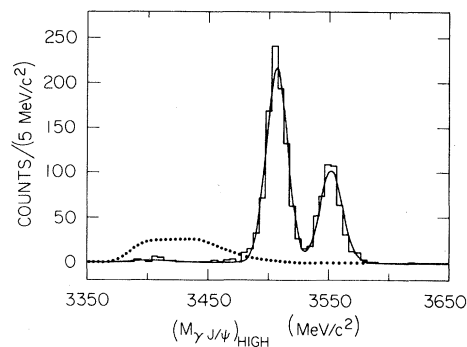


FIG. 13. Higher- $\gamma J/\psi$ -mass distribution for final  $\chi$  event sample,  $\pi^0$  and  $\eta$  subtracted. The dotted line is the expected  $\pi^0\pi^0$  background magnified 100 times.

state reported<sup>7</sup> at  $3.455 \text{ GeV}/c^2$ .

The populous states at  $\gamma J/\psi$  masses of  $3.55$  and  $3.51 \text{ GeV}/c^2$  contain 479 and 943 events, respectively. Three of the 20 events comprising the structure at  $3.41 \text{ GeV}/c^2$  are expected to arise from  $\pi^0\pi^0$  contamination. The position of  $\chi(3.41)$  is near enough to the kinematic limit where the two photon energies are equal, and therefore the projection onto the  $\gamma J/\psi$ -mass axis suffers from a kinematic reflection which alters the apparent line shape. The  $E_\gamma > 40 \text{ MeV}$  cut restricts  $M_{\gamma J/\psi}$  to the range  $3129$  to  $3644 \text{ MeV}/c^2$ ; in this region we find no evidence for a fourth  $\chi$  state.

### H. Branching ratios

The branching ratio for a particular  $\psi'$  decay channel is obtained by dividing the number of events observed in the channel, corrected for detection efficiency using the efficiencies in Table II and those for photon conversion and charged particle identification, by the total number of  $\psi'$  produced ( $N'$ ). Because of the large solid angle covered with high trigger efficiency in our detector, we choose to calculate  $N'$  from the total number of triggers, which is comprised of triggers from  $\psi' \rightarrow \text{hadrons}$  ( $N'_h$ ) and  $e^+e^- \rightarrow \text{hadrons}$  ( $N'_{nr}$ ), with  $N_h = N'_h + N'_{nr}$ ;  $e^+e^- \rightarrow e^+e^-$ , and other QED triggers which can be neglected;  $\psi'$  leptonic and semileptonic triggers; and backgrounds from degraded SPEAR electrons, beam gas collisions, and cosmic rays. QED triggers are easily removed from the trigger sample by flagging the events having a total measured energy equal to approximately the center-of-mass SPEAR energy and having back-to-back tracks. The muonic QED events are small in number and are therefore neglected.

The cosmic ray background can be categorized as muons which pass through the cavity in the center of the NaI(Tl) ball, muons which traverse a single continuous path through NaI(Tl), and cosmic electron showers. Events belonging to the second and third classes produce highly asymmetric event patterns. These backgrounds were identified by comparing the total energy deposited in the NaI(Tl) ( $E_{\text{tot}}$ ) with the asymmetry of the event, defined as  $|\sum E_i \hat{n}_i| / E_{\text{tot}}$  for  $E_i$  the measured energy in track  $i$  having direction cosines  $\hat{n}_i$ . Figure 14 shows the asymmetry versus  $E_{\text{tot}}$  scatter plot for the triggers surviving the QED rejection criteria. Cosmic rays traversing the central cavity appear quite symmetric and tend to deposit about  $400 \text{ MeV}$  in the NaI(Tl), accounting for the high

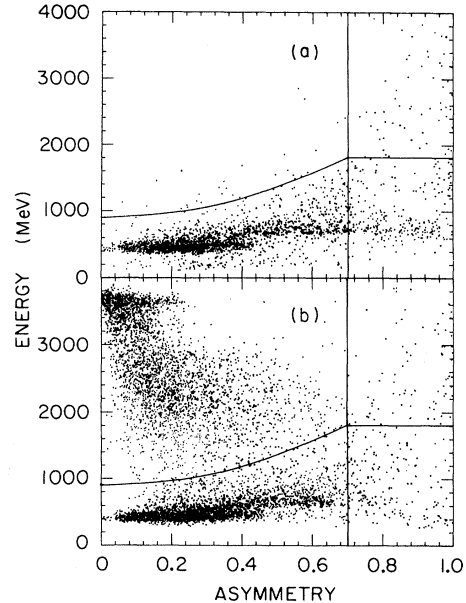


FIG. 14. Total event energy versus asymmetry (see text) plots for (a) separated and (b) colliding beams. Cuts designed to remove QED events have been applied to the events shown here.

density cluster in the lower left portion of the plots. Cosmic rays of the second class traverse more NaI(Tl) and therefore deposit about  $600 \text{ MeV}$ ; these events are fairly asymmetric and account for the cluster just above the previous one and extending to higher asymmetry values. Roughly 10% of the cosmic rays shower; such events have ill-defined energies and tend to be extremely asymmetric.

Using Fig. 14, a boundary can be constructed, as shown on the figure, which clearly separates the backgrounds from the other triggers. The number of background-free triggers,  $N_t$ , is obtained by correcting the events in the upper left region of Fig. 14(b) for leakage across the boundaries. Leakage of the backgrounds across the boundary into the good event region is less than 1%; the  $900\text{-MeV}$  threshold of the boundary in the high-symmetry region of Fig. 14(b) has been shown by a Monte Carlo study to exclude 3% of the known  $\psi'$  decays. Since the boundaries are established from a comparison of colliding-beam data with that for separated beams, a conceivable change of geometry in the beams after separation causes us to place a conservative uncertainty of 10% on  $N_t$  obtained in the above manner. The number of  $\psi'$  is finally obtained as  $N' = N_t - N_{nr} = (7.76 \pm 0.78) \times 10^5$ , where  $N_{nr}$  is calculated from the total integrated luminosity and  $\sigma(e^+e^- \rightarrow \text{hadrons}) = 2.5\sigma(e^+e^- \rightarrow \mu^+\mu^-)$

at  $E_{c.m.} = 3.7$  GeV.

The branching ratio for the decay of the  $J/\psi$  into dileptons is taken as<sup>22</sup>

$$B(J/\psi \rightarrow l^+l^-) = 2 \times (0.069 \pm 0.009);$$

it is the dominant systematic error (13%) in this experiment. Combined in quadrature with the uncertainty on  $N'$ , an overall systematic uncertainty of 16% is obtained. The branching ratios shown in Table III are then obtained for the processes (4.1) and (4.2). A comparison of the branching-ratio results in Table III with previous experiments can be found in Table IV.

The first error on  $M(\chi)$  in Table III covers uncertainties arising from statistics, the NaI(Tl) energy line shape, our knowledge of the  $J/\psi - \psi'$  mass difference, and our acceptance. The systematic error on the  $\chi(3.51)$  and  $\chi(3.55)$  masses is dominated by the 4-MeV/ $c^2$  uncertainty in  $M_{J/\psi}$ . To within a few percent the values for  $M_\chi$  scale as  $\Delta[M_\chi] = \Delta[M_{J/\psi}]$ , for  $(M_\psi - M_{J/\psi})$  constant. The Particle Data Tables present an average  $J/\psi$  mass of  $3097 \pm 1$  MeV/ $c^2$ . If this value is used, our values obtained for the  $\chi$  masses must be increased by 2.0 MeV; in both cases the 4.0 MeV/ $c^2$   $J/\psi$  mass uncertainty is reduced to 0.8 MeV/ $c^2$ . Details are described in Appendix H of Ref. 10.

The three candidates for the  $2^1S_0$  with reported masses of 3455 (Ref. 3), 3591 (Ref. 7), and 3592 MeV/ $c^2$  (Ref. 8) have not been confirmed in this experiment; only 90%-C.L. upper limits on the cascade branching ratios are obtained. For the state reported at 3.455 GeV/ $c^2$  only the data from our  $\mu^+\mu^-$  data is used to obtain the upper limit

(this is discussed in Sec. IV G). We note that models for the hyperfine splitting in charmonium predict<sup>24</sup> a  $2^1S_0$  mass near 3.6 GeV/ $c^2$ , with a cascade branching ratio less than  $10^{-6}$  provided that 2978 MeV/ $c^2$  is the correct  $1^1S_0$  mass.<sup>5</sup> Such a cascade branching ratio is more than an order of magnitude below the sensitivity of this experiment; this upper-limit branching ratio is also consistent with the initial observation<sup>8</sup> of the state with a mass of 3592 MeV/ $c^2$ .

The direct decay  $\psi' \rightarrow \gamma\gamma J/\psi$  has been calculated by Pelaquier and Renard.<sup>25</sup> They find that the branching ratio for the direct decay should be less than  $3 \times 10^{-3}$ , but give no  $\gamma\gamma$  mass structure for the decay. There are no events in the  $\mu^+\mu^-$  final state Dalitz plot which cannot be attributed to the  $1^3P_{012}$  states or  $\pi^0$  and  $\eta$  decay modes of the  $\psi'$ . A 90%-C.L. upper limit on the direct-decay branching ratio of  $2 \times 10^{-3}$  results for a uniformly distributed Dalitz plot.

#### I. $\chi$ -cascade angular-correlation analysis

The particles participating in the sequence

$$e^+e^- \rightarrow \psi', \quad (4.6a)$$

$$\psi' \rightarrow \gamma'\chi, \quad (4.6b)$$

$$\chi \rightarrow \gamma J/\psi, \quad (4.6c)$$

$$J/\psi \rightarrow l^+l^-, \quad (4.6d)$$

define the frames shown in Figure 15. The sign of the outgoing-lepton charges is not measured in our nonmagnetic detector, thereby necessitating a ran-

TABLE III. Crystal Ball results. The first error is the statistical error + acceptance. The second error is systematic.

State $\chi$ mass (MeV/ $c^2$ )	Branching ratio (%) $B(\psi' \rightarrow \gamma\chi \rightarrow \gamma\gamma J/\psi)$	
3553.9 $\pm$ 0.5 $\pm$ 4	1.26 $\pm$ 0.08 $\pm$ 0.20	
3508.4 $\pm$ 0.4 $\pm$ 4	2.38 $\pm$ 0.12 $\pm$ 0.38	
3413 (Ref. 23)	0.059 $\pm$ 0.015 $\pm$ 0.009	
3455 (Ref. 3)	< 0.02	90% confidence level
3591 (Ref. 7)	< 0.04	
Particle "m"	$B(\psi' \rightarrow mJ/\psi)$	
$\eta$	2.18 $\pm$ 0.14 $\pm$ 0.35	
$\pi^0$	0.09 $\pm$ 0.02 $\pm$ 0.01	

TABLE IV. Comparison with other experiments. Limits are at 90% confidence level. Crystal Ball masses are denoted by an asterisk, Mark II masses by a double asterisk. There is an additional 4-MeV/ $c^2$  error on all the masses.

State (MeV/ $c^2$ )	Crystal Ball	Mark II <sup>6</sup>	Mark I <sup>3</sup>	DESY-Heidelberg <sup>7</sup>
$B(\psi' \rightarrow \gamma\gamma J/\psi)$ (%), or 90%-C.L. upper limit				
$\chi(3553.9 \pm 0.5)^*$	$1.26 \pm 0.22$	$1.1 \pm 0.3$	$1.0 \pm 0.6$	$1.0 \pm 0.2$
$\chi(3508.4 \pm 0.4)^*$	$2.38 \pm 0.40$	$2.4 \pm 0.6$	$2.4 \pm 0.8$	$2.5 \pm 0.4$
$\chi(3412.9 \pm 0.6)^{**}$	$0.06 \pm 0.02$	$< 0.56$	$0.2 \pm 0.2$	$0.14 \pm 0.09$
$\chi(3455)$	$< 0.02$	$< 0.13$	$0.8 \pm 0.4$	$< 0.25$
$\chi(3591)$	$< 0.04$	—	—	$0.18 \pm 0.06$
$B(\psi' \rightarrow mJ/\psi)$ (%)				
$\eta$	$2.18 \pm 0.38$	$2.5 \pm 0.6$	$4.3 \pm 0.8$	$3.6 \pm 0.5$
$\pi^0$	$0.09 \pm 0.03$	$0.15 \pm 0.06$	—	—

dom charge assignment in both the data and in the Monte Carlo simulations used to analyze the data. The angular distribution function  $W(\cos\theta', \phi', \cos\theta_{\gamma\gamma}, \cos\theta, \phi, \vec{p})$  (Ref. 26) describing the sequence (4.6) is a function of the five angles shown schematically in Fig. 15 and of the multipole parameters  $\vec{p}$  described in Ref. 26 and at the end of this section. The polar angles of  $e^+$  in the

laboratory frame are denoted by  $\theta'$  and  $\phi'$ , with the polar axis taken along the  $\gamma'$  direction, and with  $\hat{y}$  orthogonal to the two photon directions. Similarly,  $\theta$  and  $\phi$  describe one of the outgoing-lepton directions in the  $J/\psi$  rest frame, with  $\hat{z}$  along the direction of  $\gamma$ . The angle between the photons in the  $\chi$  rest frame is  $\theta_{\gamma\gamma}$ . Vectors used to obtain these angles are measured in different frames accordant with the calculation of  $W$ ; they can be defined using the unit vectors  $\hat{e}^+$  (the incident positron) and  $\hat{\gamma}'$  in the  $\psi'$  rest frame;  $\hat{\gamma}'$ ,  $\hat{\gamma}$  in the  $\chi$  rest frame; and  $\hat{l}^+$  (the final positive lepton) and  $\hat{\gamma}$  in the  $J/\psi$  rest frame. Details concerning the boosts and rotations can be found in Ref. 10. Then,

$$\begin{aligned}
 \cos\theta' &= \hat{e}^+ \cdot \hat{\gamma}', & \cos\theta_{\gamma\gamma} &= \hat{\gamma}' \cdot \hat{\gamma}, \\
 \tan\phi' &= \frac{\hat{e}^+ \cdot (\hat{\gamma}' \times \hat{\gamma})}{\hat{e}^+ \cdot [(\hat{\gamma}' \times \hat{\gamma}) \times \hat{\gamma}']}, \\
 \cos\theta &= \hat{l}^+ \cdot \hat{\gamma}, \\
 \tan\phi &= \frac{\hat{l}^+ \cdot (\hat{\gamma}' \times \hat{\gamma})}{\hat{l}^+ \cdot [(\hat{\gamma}' \times \hat{\gamma}) \times \hat{\gamma}]}.
 \end{aligned} \tag{4.7}$$

The data is analyzed by means of a histogram over the five angles. It has been pointed out by Tanenbaum *et al.*<sup>27</sup> that the statistics for each histogram bin are enhanced if parity conservation is used to restrict the range of some variables. Each of the four decays (4.6) involved in the cascade conserves parity in the appropriate rest frame. Given values for the five angles in a particular event, transformations<sup>10</sup> are applied to the data to produce a set of angles in which  $\cos\theta'$ ,  $\cos\theta_{\gamma\gamma}$ ,

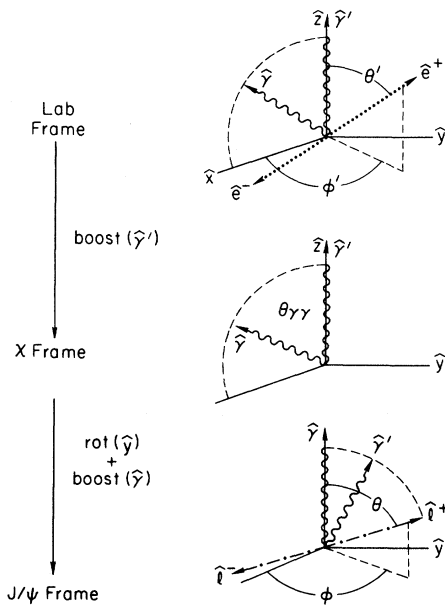


FIG. 15. Vectors and frames describing the cascade reaction  $\psi' \rightarrow \gamma'\chi$ ,  $\chi \rightarrow \gamma J/\psi$ ,  $J/\psi \rightarrow l^+l^-$ . In the laboratory frame  $e^\pm$  refer to the beam electrons; in the  $J/\psi$  frame  $l^\pm$  refer to the outgoing leptons.

$\cos\theta$ , and  $\phi'$  all have positive values and the distribution  $W$  is left unaltered. The decision to choose  $\phi$  as the variable with full-range values was arbitrary.

The multipole coefficients are defined by the relation

$$\Gamma(\chi \rightarrow \gamma J / \psi) \propto \sum_{j=1}^{J_x+1} (a_j)^2, \quad (4.8)$$

and similarly for  $\Gamma(\psi' \rightarrow \gamma \chi)$ . The multipole coefficients are  $a_j$ ; in this analysis we normalize their sum of squares to unity. If the  $\chi$  parity is even,  $a_1$  corresponds to an  $E1$  transition,  $a_2$  to  $M2$ , and  $a_3$  to  $E3$ . The explicit forms of the multipole coefficients are given in Ref. 26. For a  $\chi$  with spin  $J_x$  there are  $J_x + 1$  multipole amplitudes which describe the radiative decays (4.6b) and (4.6c). Given the standard charmonium model,<sup>1</sup> one expects that the low-order multipole amplitudes dominate. Therefore, the octupole coefficient possible in the spin-2 case was ignored; it would have been considered had the quadrupole amplitude proven significant. The parameter vector is therefore written as  $\vec{p} = (J_x, a', a)$  where  $a'$  and  $a$  describe the multipole structure for the radiative transitions (4.6b) and (4.6c), respectively. The proportions of the various  $a_j$ , in addition to the  $\chi$  spin  $J_x$ , are measured by comparing calculated  $W$  distributions with the data.

### 1. Spin analysis

Before performing the general analysis, which involves binning in all five angles, it is worth carrying out a simpler procedure which gives information on the spin of the  $\chi$  states. Some spin information on the  $\chi$  spin has already been obtained from the observation of certain hadronic decay modes of the  $\chi$ , and in fact this information is required in addition to the spin information from our analysis in order to determine the  $\chi$  parities. In particular, it is observed that  $\chi(3.55)$  and  $\chi(3.41)$  decay frequently into  $\pi^+\pi^-$  and  $K^+K^-$  while  $\chi(3.51)$  does not.<sup>27</sup> Since both these decay products are pseudoscalar ( $J^P=0^-$ ), one concludes that  $\chi(3.55)$  and  $\chi(3.41)$  have  $J^{PC}=0^{++}$  or  $2^{++}$ . The  $\chi(3.51)$  state is observed to decay into  $\pi^+K^-K_S$  (Ref. 21) (three pseudoscalars) so  $0^+$  is not a possible assignment. Failure of the  $\chi(3.51)$  to decay into two pseudoscalars suggests an unnatural spin-parity ( $0^-, 1^+, 2^-$ ).

The simplified procedure uses certain projections of the five dimensional space to provide informa-

tion on the spin of the  $\chi$  states. Our Monte Carlo studies for the spin hypotheses 0,1,2 and several multipole configurations have determined that  $\cos\theta'$  and  $\cos\theta$  are useful for this purpose. Figures 16(a) and 16(b) show data for the  $\chi(3.51)$  and  $\chi(3.55)$  with suitably normalized Monte Carlo curves<sup>28</sup> for the plausible spin hypotheses; there is insufficient data for  $\chi(3.41)$  to draw meaningful conclusions. Although the  $\chi(3.55)$  data fits a spin-0 curve rather poorly and spin 2 somewhat better, the evidence from the projection does not present an overwhelming case for an assignment of spin 2. The  $\chi(3.51)$  is fairly well established to have spin 1 on the basis of the  $\cos\theta'$  projection.

### 2. Multipole analysis

The maximum-likelihood fit over all variables enables one to combine the information from all projections, thereby establishing spin assignment with far greater assurance. The five dimensional histogram over  $\cos\theta'$ ,  $\phi'$ ,  $\cos\theta_{\gamma\gamma}$ ,  $\cos\theta$ , and  $\phi$  was formed by dividing the variables with only positive ranges into three equal bins, and  $\phi$  into six bins; a total of 486 bins resulted. Each spin-multipole hypothesis required calculation of a binned Monte Carlo simulation which was acceptance corrected and constrained to have a total number of events

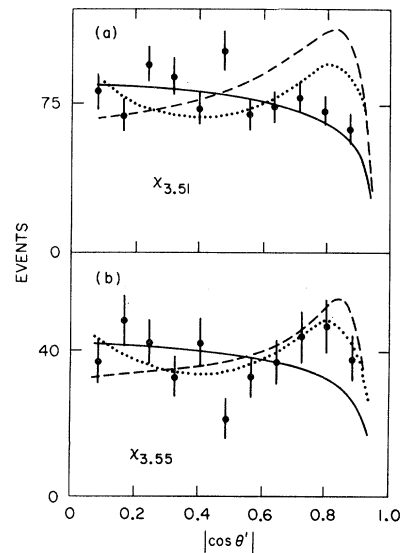


FIG. 16. Projections of  $\cos\theta'$  for (a)  $\chi(3.51)$  data and (b)  $\chi(3.55)$  data. Shown on the plots are the Monte Carlo simulations (normalized to the data) for the hypotheses  $J=0$  (dashed),  $J=1$  (solid), and  $J=2$  (dotted).

equal to that in the experimental data sample. A binomial probability density function describes the probability for observing a given number of events in any particular bin.

The data for the  $\chi$  states was separated from the other  $\gamma\gamma J/\psi$  data by applying the  $\eta$  and  $\pi^0$  cuts described in Table II. The individual  $\chi$  states were then separated by cutting on  $(M_{\gamma J/\psi})_{\text{high}}$  with 95% and 90% windows for  $\chi(3.509)$  and  $\chi(3.554)$ , respectively; 921 events for the  $\chi(3.51)$  and 441 events for the  $\chi(3.55)$  then comprised the individual data samples. Because of their different acceptances the  $e^+e^-$  and  $\mu^+\mu^-$  final states were separately compared to Monte Carlo simulations for the two final states, and then the electron and muon Monte Carlo histograms were added together when the likelihood function was calculated. The experimental data was therefore binned directly, with the acceptance factors built into the Monte Carlo simulations.

The results from the likelihood fit are presented in Table V, where the significance of each fit is compared to the best fit ( $L_{\text{max}}$ ) by means of the ratio of likelihoods  $L/L_{\text{max}}$ . Plots of the likelihood function as a function of  $a_2$  and  $a'_2$ , for the optimal spin assignments, are shown in Fig. 17. The normalization of the multipole amplitudes limits the range of  $a_2$  and  $a'_2$  to  $[-1, +1]$ . The notation of Ref. 27 is adopted in describing the dipole-quadrupole mixing in (4.6b) and (4.6c):  $D$ , pure dipole,  $a_2(a'_2)=0$ ;  $Q$ , pure quadrupole,  $a_2(a'_2)=1$ ;  $D+Q$ , equal mixture with positive sign,  $a_2(a'_2)=+1/\sqrt{2}$ ;  $D-Q$ , equal mixture with negative sign,  $a_2(a'_2)=-1/\sqrt{2}$ . The contours of the likelihood function  $L$  are plotted at  $L_{\text{max}}\exp(-n^2/2)$  intervals, with each level below the main peak approximately representing a successive  $1\sigma$  departure from optimization; the interpretation of  $\sigma$  as a Gaussian standard deviation breaks down for large displacements from the maxima. These contour

levels form the grids in Fig. 17; the corresponding contour maps are shown in Fig. 18. The multiplicities of the radiative transitions for  $\chi(3.55)$  and  $\chi(3.51)$  are thus found to be predominantly dipole in nature. Earlier analysis<sup>27</sup> also found this to be the case for the  $\chi(3.51)$ , but only when its spin was assumed to be 1. The data from the analysis in this new study yield high confidence levels for the spin and multipole assignments preferred in the standard charmonium model; in particular, spin 2 for  $\chi(3.51)$  is ruled out.

## V. CONCLUSIONS AND DISCUSSION

Our analysis of the  $\gamma\gamma J/\psi$  data, together with previous measurements, permits us to make the following conclusions.

(1) Between the  $\psi'$  and  $J/\psi$  only three states have been observed and confirmed in a study of the cascade reaction. States with masses (Crystal Ball) of  $3.554 \pm 0.004$  and  $3.508 \pm 0.004$   $\text{GeV}/c^2$  have large branching ratios into  $\gamma J/\psi$  and quantum numbers  $J^{PC}=2^{++}$  and  $1^{++}$ , respectively. These characteristics are determined from an analysis of the angular correlations in the cascade decay and from the existence of some hadronic decay modes. A state with a mass<sup>23</sup>  $3.413 \pm 0.004$   $\text{GeV}/c^2$  has a small branching ratio into  $\gamma J/\psi$ .

(2) Our analysis of a sample of  $8 \times 10^5$   $\psi'$  decays finds no additional state in the mass range  $3.129 - 3.644$   $\text{GeV}/c^2$ . In particular, we do not confirm states observed in previous cascade studies at masses of 3.455 (Ref. 3) and 3.591  $\text{GeV}/c^2$  (Ref. 7). We note that the theoretical cascade branching ratio for a  $2^1S_0$  state predicted<sup>24</sup> near 3.6  $\text{GeV}/c^2$  is below the sensitivity of this experiment.

(3) The multipolarity of the radiative transitions between the  $2^3S_1$  and  $1^3P_{12}$  states is measured to be predominantly electric dipole.

TABLE V. Results of likelihood fit.

Hypothesis	$-2 \ln(L/L_{\text{max}})$	$a'_2$	$a_2$
$\chi(3.51)$ data:			
$J_\chi=1$	0	$+(0.077^{+0.050}_{-0.045})$	$-(0.002^{+0.020}_{-0.008})$
$J_\chi=2$	16		
$J_\chi=0$	162		
$\chi(3.55)$ data:			
$J_\chi=2$	0	$+(0.132^{+0.098}_{-0.075})$	$-(0.333^{+0.292}_{-0.116})$
$J_\chi=1$	20		
$J_\chi=0$	40		

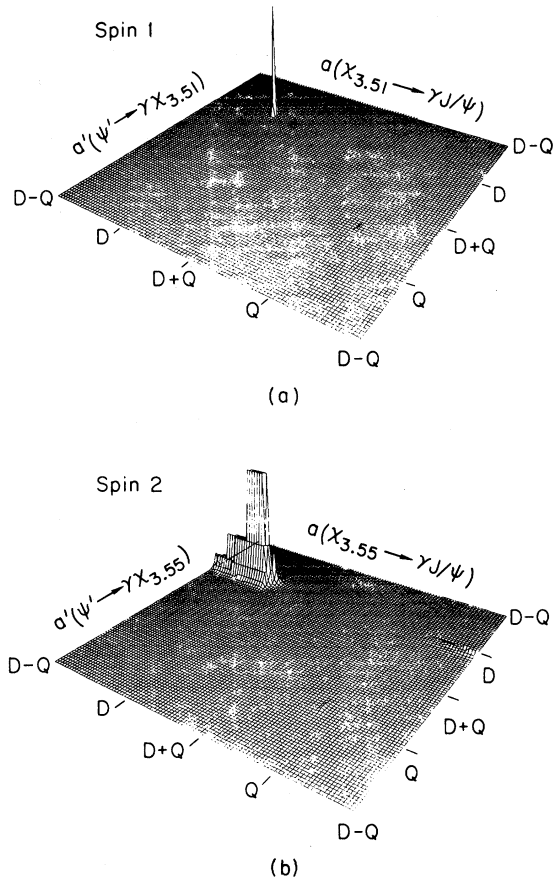


FIG. 17. Likelihood function for (a)  $\chi(3.51)$  data with  $J=1$  hypothesis, and (b)  $\chi(3.55)$  data with  $J=2$  hypothesis. Vertical contours are plotted at nominal Gaussian deviations from the maximum value (see text).

(4) Our measurement of  $\psi' \rightarrow \eta J/\psi$  obtains a branching ratio which is smaller than earlier accepted values,<sup>3,7</sup> but which is in agreement with the latest Mark II result.<sup>6</sup> The branching ratio remains surprisingly large, indicating a  $c\bar{c}$  component<sup>29</sup> in the  $\eta$  or a large gluonic coupling<sup>30</sup> for the  $\eta$  to charmed quarks.

(5) The decay  $\psi' \rightarrow \pi^0 J/\psi$ , which violates isospin symmetry, is observed both in this experiment and in a Mark II experiment.<sup>6</sup> Citing early evidence (such as the decays  $\eta \rightarrow 3\pi$ ) that strong isospin is broken at some level, Segre and Wyers<sup>31</sup> first suggested that the  $\eta$  can convert into a physical  $\pi^0$  by means of  $\pi$ - $\eta$  mixing [SU(2) breaking], thus permitting the decay  $\psi' \rightarrow \pi^0 J/\psi$ . More recent work has revealed that the decay is augmented by contributions from a virtual  $\eta'$  (Ref. 32) and a direct  $\pi^0$  coupling<sup>33</sup>; in the last several years more models<sup>34</sup>

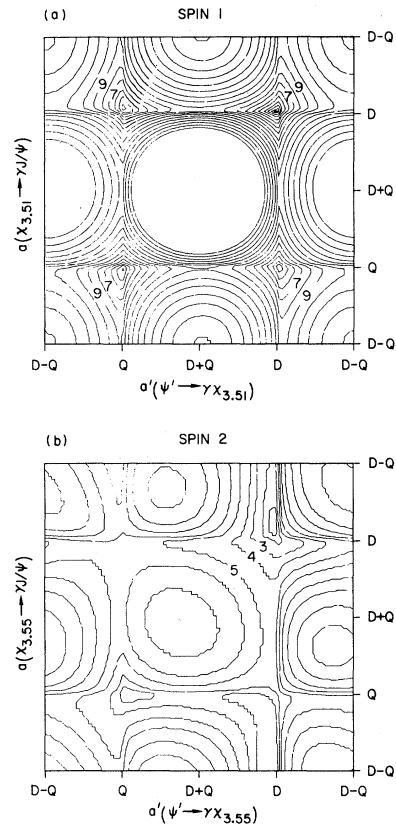


FIG. 18. Contour maps corresponding to Fig. 17. Contour 0 is taken at the maximum value of the likelihood function  $L$ .

have appeared, all in reasonable agreement with the data.

#### ACKNOWLEDGMENTS

We gratefully acknowledge the efforts of A. Baumgarten and J. Broeder of SLAC, and B. Beron, E. B. Hughes, and R. Parks of HEPL, Stanford University, as well as those of the LINAC and SPEAR staffs at SLAC. This work was supported by the Department of Energy under Contracts Nos. DE-AC-3-76SF00515 (SLAC), EY-76-CO2-3064 (Harvard), and EY-76-CO3-0068 (CIT), and by the National Science Foundation contracts PHY78-00967 (HEPL), PHY78-07343 (Princeton), and PHY75-22980 (CIT). Support for individuals came from the institutions listed, as well as NATO Fellowship (H.K., Federal Republic of Germany), Chaim Weizmann Fellowship (F.P.), and the Sloan Foundation (T.B.).

- \*Present address: Enrico Fermi Institute, University of Chicago, Chicago, Illinois 60637.
- †Present address: Max Planck Institute for Physics and Astrophysics, D-8000 Munich (40), Federal Republic of Germany.
- ‡On leave from the Institute of High Energy Physics, Academia Sinica, People's Republic of China.
- §Present address: Wentorfer Strasse 149, D-2050 Hamburg, Federal Republic of Germany.
- ||Present address: Department of Physics, University of Cape Town, Cape Town, South Africa.
- ¶Present address: Physics Department, University of Washington, Seattle, Washington, 98195.
- \*\*Present address: SCIPP, University of California at Santa Cruz, Santa Cruz, California 95064.
- ††Present address: University of Bonn, Bonn, Federal Republic of Germany.
- ‡‡Present address: Schlumberger-Doll Research Center, Ridgefield, Connecticut 06877.
- §§Present address: Systems Control Technology, Palo Alto, California 94304.
- <sup>1</sup>T. Appelquist and H. Politzer, *Phys. Rev. Lett.* **34**, 43 (1975).
- <sup>2</sup>A. Boyarski *et al.*, *Phys. Rev. Lett.* **34**, 1357 (1975); V. Lüth *et al.*, *Phys. Rev. Lett.* **35**, 1124 (1975).
- <sup>3</sup>J. Whitaker *et al.*, *Phys. Rev. Lett.* **37**, 1596 (1976).
- <sup>4</sup>W. Braunschweig *et al.*, *Phys. Lett.* **57B**, 407 (1975); G. Feldman *et al.*, *Phys. Rev. Lett.* **35**, 821 (1975).
- <sup>5</sup>R. Partridge *et al.*, *Phys. Rev. Lett.* **45**, 1150 (1980).
- <sup>6</sup>T. M. Himel *et al.*, *Phys. Rev. Lett.* **45**, 1146 (1980).
- <sup>7</sup>W. Bartel *et al.*, *Phys. Lett.* **79B**, 492 (1978).
- <sup>8</sup>F. C. Porter *et al.*, *Phys. Rev. Lett.* **48**, 70 (1982).
- <sup>9</sup>C. Peck and F. Porter, Crystal Ball Report No. CB-NOTE 010, 1976 (unpublished).
- <sup>10</sup>M. Oreglia, Ph.D. thesis, Stanford University Report No. SLAC-226, 1980 (unpublished).
- <sup>11</sup>J. Gaiser *et al.*, *IEEE Trans. Nucl. Sci.* **NS-26**, 173 (1979).
- <sup>12</sup>F. Bulos, Crystal Ball Report No. CB-NOTE 117, 1976 (unpublished).
- <sup>13</sup>J. Tompkins, Crystal Ball Report No. CB-NOTE 232, 1977 (unpublished).
- <sup>14</sup>G. Godfrey, Crystal Ball Report No. CB-NOTE 121, 1976 (unpublished).
- <sup>15</sup>Shower fluctuation and hadronic interactions sometimes cause neighboring modules to measure a larger energy than the central module.
- <sup>16</sup>Two masses may be formed with the  $J/\psi$  and either one of the photons, the lower-energy photon yielding a higher mass solution than its partner.
- <sup>17</sup>W. Tanenbaum *et al.*, *Phys. Rev. Lett.* **36**, 402 (1976).
- <sup>18</sup>M. Oreglia *et al.*, *Phys. Rev. Lett.* **45**, 959 (1980).
- <sup>19</sup>The values 3095.0 and 3684.0 MeV/ $c^2$  were used for the  $J/\psi$  and  $\psi'$  masses, respectively, in the fitting program.
- <sup>20</sup>Particle Data Group, *Rev. Mod. Phys.* **52**, S1 (1980).
- <sup>21</sup>T. M. Himel *et al.*, *Phys. Rev. Lett.* **44**, 920 (1980).
- <sup>22</sup>A. Boyarski *et al.*, *Phys. Rev. Lett.* **34**, 1357 (1975).
- <sup>23</sup>T. M. Himel, Ph.D. thesis, Stanford University Report No. SLAC-223, 1979 (unpublished). The mass of  $\chi(3.41)$  is established as  $3412.9 \pm 0.6 \pm 4$  MeV/ $c^2$  from its hadronic decays.
- <sup>24</sup>C. Quigg, in *Proceedings of the 1979 International Symposium on Lepton and Photon Interactions at High Energy, Fermilab*, edited by T. B. W. Kirk and H. D. I. Abarbanel (Fermilab, Batavia, Illinois, 1980) p. 239.
- <sup>25</sup>E. Pelaquier and F. Renard, *Nuovo Cimento* **32A**, 421 (1976).
- <sup>26</sup>G. Karl, S. Meshkov and J. Rosner, *Phys. Rev. D* **13**, 1203 (1976).
- <sup>27</sup>W. Tanenbaum *et al.*, *Phys. Rev. D* **17**, 1731 (1978).
- <sup>28</sup>For this comparison the helicity amplitudes in the Monte Carlo simulations were fixed assuming lowest-order-multipole dominance.
- <sup>29</sup>H. Harari, *Phys. Lett.* **60B**, 172 (1975); H. Fritzsch and J. D. Jackson, *Phys. Lett.* **66B**, 365 (1977).
- <sup>30</sup>H. Goldberg, *Phys. Rev. Lett.* **44**, 363 (1980).
- <sup>31</sup>G. Segre and J. Weyers, *Phys. Lett.* **62B**, 91 (1976).
- <sup>32</sup>H. Genz, *Lett. Nuovo Cimento* **21**, 270 (1978).
- <sup>33</sup>P. Langacker, *Phys. Lett.* **90B**, 447 (1980).
- <sup>34</sup>N. Deshpande and E. Ma, *Phys. Lett.* **69B**, 343 (1977); R. Bhandari and L. Wolfenstein, *Phys. Rev. D* **17**, 1852 (1978); N. Isgur *et al.*, *Phys. Lett.* **89B**, 79 (1979); N. Isgur, *Phys. Rev. D* **12**, 3720 (1979); N. Isgur *et al.*, *Phys. Lett.* **89B**, 79 (1979); T. Pham, Ecole Polytechnique Report No. 80-0330, 1980 (unpublished); B. L. Ioffe and M. A. Shifman, *Phys. Lett.* **95B**, 99 (1980).